Strong Coupling of Plasmon and Nanocavity Modes for Dual-Band, Near-Perfect Absorbers and Ultrathin Photovoltaics

Carl Hägglund,[*,†,‡] Gabriel Zeltzer,[§,∥,⊥] Ricardo Ruiz,[§,⊥] Artit Wangperawong,[△,#] Katherine E. Roelofs,[□] and Stacey F. Bent[*,†]

†Department of Chemical Engineering, △Department of Electrical Engineering, and □Department of Materials Science and Engineering, Stanford University, Stanford, California 94305, United States
§HGST, a Western Digital Company, San Jose, California 95135, United States

S Supporting Information

ABSTRACT: When optical resonances interact strongly, hybridized modes are formed with mixed properties inherited from the basic modes. Strong coupling therefore tends to equalize properties such as damping and oscillator strength of the spectrally separate resonance modes. This effect is here shown to be very useful for the realization of near-perfect dual-band absorption with ultrathin (~10 nm) layers in a simple geometry. Absorber layers are constructed by atomic layer deposition of the heavy-damping semiconductor tin mono-sulfide (SnS) onto a two-dimensional gold nanodot array. In

combination with a thin (55 nm) SiO_2 spacer layer and a highly reflective Al film on the back, a semiopen nanocavity is formed. The SnS-coated array supports a localized surface plasmon resonance in the vicinity of the lowest order antisymmetric Fabry–Perot resonance of the nanocavity. Very strong coupling of the two resonances is evident through anticrossing behavior with a minimum peak splitting of 400 meV, amounting to 24% of the plasmon resonance energy. The mode equalization resulting from this strong interaction enables simultaneous optical impedance matching of the system at both resonances and thereby two near-perfect absorption peaks, which together cover a broad spectral range. When paired with the heavy damping from SnS band-to-band transitions, this further enables approximately 60% of normal incident solar photons with energies exceeding the band gap to be absorbed in the 10 nm SnS coating. Thereby, these results establish a distinct relevance of strong coupling phenomena to efficient, nanoscale photovoltaic absorbers and more generally for fulfilling a specific optical condition at multiple spectral positions.

KEYWORDS: strong interaction, plasmonic solar cells, tin monosulfide, atomic layer deposition, localized surface plasmon resonances, vacuum Rabi splitting
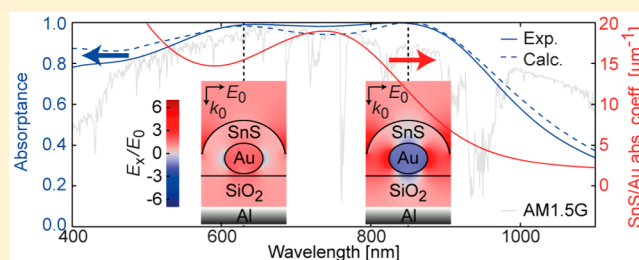
In pursuit of thinner, more efficient, and ultimately cheaper solar cells, both localized and propagating surface plasmon resonances in metal nanostructures have been explored for their ability to trap and couple light to useful charge carrier generation in thin semiconductor layers.[1,2] Out of several routes, one of the more promising ones makes use of the strong electromagnetic near-field sustained around metal nanoparticles upon excitation of their localized surface plasmon resonances (LSPRs).[3−5] The enhanced near-field allows for the plasmon energy to be transferred to band-gap excitations in nearby semiconductor material. This effect can be extended beyond hot spots around single nanoparticles to nanoparticle arrays and other two-dimensional structures. However, a high optical damping of the semiconductor (as expressed by a high value for the product of its refractive index and extinction coefficient, or equivalently a high imaginary part of its permittivity) relative to the metal damping is a key factor for favoring the generation of long-lived electron−hole pairs in the semiconductor over Joule heating losses in the metal.[6]

In parallel development, nanocavity designs have been explored for an optical domain realization of the Salisbury screen.[7] Such optical nanocavities comprise an ultrathin (~10 nm) absorber layer on top of a transparent spacer layer and a highly reflective layer on the rear. Under favorable conditions, and for a particular wavelength, the layer thicknesses may be chosen such that the stack realizes the condition for optical impedance matching, where the overall reflectance is completely eliminated through destructive interference of partially reflected waves. Since transmission is blocked at the rear, essentially all light is then channeled into the absorber layer.[5,8−12] Optical impedance matching can also be realized if the spacer is replaced by a reflector with a metasurface design that enables control of the phase shift of the back reflected wave.[13] In the simplest case even a plain metal film, without a spacer layer on top, is adequate.[14] These types of low-quality-

factor, semiopen nanocavities can support an antisymmetric Fabry−Perot (FP) resonance that is spectrally broadband and insensitive to the angle of incidence.[5,12,14]

The combination of plasmonic arrays and nanocavities provides a versatile platform for broadband, high optical absorption,[15−19] as well as for antireflective layers.[20] For these applications, it is generally favorable to introduce as many resonance modes as possible in the spectral range targeted.[21,22] However, for broadband absorber layers, limitations may arise from fabrication constraints or from a desire to minimize the absorber layer thickness or its complexity. If the design has few degrees of freedom, simultaneous optical impedance matching of several resonances becomes challenging.

In this work, we introduce the strong interaction and resultant mixing of basic modes into new, hybridized resonance modes as an opportunity to collectively tune a system to conditions for high absorption at two or more spectral positions. This is experimentally demonstrated using a tin monosulfide (SnS)-coated gold nanodot array constituting an ultrathin absorber layer as well as the top layer of a semiopen nanocavity (Figure 1). Although SnS is a semiconductor with a
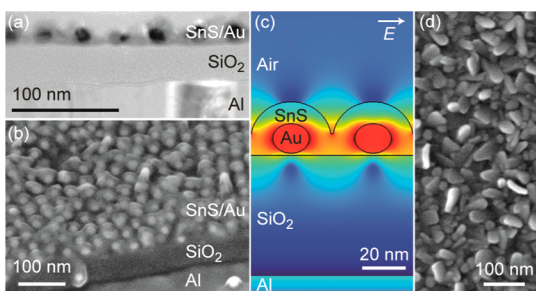

Figure 2. (a) Damping of a 350 nm thick film of VTD SnS, compared to typical thin film solar cell materials and other semiconductors, including an ALD-grown SnS_x film with $x \approx 2$. (b) Damping of VTD SnS compared to crystalline and ALD SnS. The anisotropic damping of crystalline (orthorhombic) SnS was reported by Eymard and Otto[29] for polarizations in the layer planes along the principal a- (E∥a) and b-axis (E∥b). A weighted average (1/3 E∥a + 2/3 E∥b) of the orthorhombic SnS matches well with the damping of the VTD SnS. For SnS films grown on Si(100) by ALD and film thicknesses as indicated, the damping is lower and strongly thickness dependent. A Bruggeman mixture of air and VTD SnS (55% filling factor in example shown) is used to approximate ALD SnS properties in the FEM calculations.

■ RESULTS AND DISCUSSION

Atomic layer deposition (ALD) of tin monosulfide onto Si(100) and glass substrates was carried out as described in the Methods section. The samples were characterized by spectroscopic ellipsometry (SE), to yield layer thicknesses and their optical properties. SnS turns out to be a rather complex material from an optical standpoint, as it grows in an anisotropic, blade-like morphology;[23,25] see Figure 1d. As noted by Kim and George,[27] nucleation of the ALD precursor Sn(II)(acac)₂, used for the studies herein, is sensitive to the substrate surface and its condition. Along with the small thicknesses studied, this contributed to a rather high variability of the optical properties. Nevertheless, the deposited material clearly absorbs strongly well into the near-infrared, in line with a band gap around 1.0 eV. This is in stark contrast to ALD using the precursor TDMASn(IV), which as a result of its higher Sn oxidation state gives SnS_2-like films with a band gap around 2.5 eV (Figure 2a).[9] The damping part of the permittivity, exemplified in Figure 2b for a few different ALD SnS thicknesses, is lower than for thicker SnS films and tends to increase with the thickness. This is likely from film densification; if roughness of the ALD SnS films is taken into account by means of a Bruggeman effective medium approximation,[28] the effective film permittivities can be brought into reasonable agreement with data for thicker SnS films grown epitaxially on NaCl by vapor transport deposition (VTD).[25] The anisotropic optical properties of crystalline SnS were previously reported by Eymard and Otto.[29] Their data for polarizations along the a- and b-axes defined in the layer planes of orthorhombic SnS are included in Figure 2b. The measured VTD film permittivity is well approximated by an average over these polarizations, if assuming that the unreported data for the crystallographic c-axis is close to that of the b-axis. Optically, the tin sulfide produced by VTD and ALD is thus close to that of orthorhombic SnS.

Figure 1. (a) Transmission electron microscopy (TEM) cross section of a sample with a SnS-coated gold nanodot array. (b) Tilted SEM view of the coated array and sublayers. (c) Geometry and electric field intensity distribution (increasing from blue to red) for the sample used in FEM calculations. In the example, light of 850 nm wavelength is incident from the top. (d) SEM image of a 500 cycle ALD SnS film on Si(100).

suitable (indirect) band gap of 1.0 to 1.1 eV for photovoltaic applications,[23−25] high-efficiency SnS solar cells have not yet been achieved. As a solar cell absorber, SnS suffers from a low minority carrier diffusion length of less than 400 nm, as well as from band misalignment in typical thin film solar cell configurations.[26] It does, however, have a very high permittivity, with an exceptionally high damping component over the visible to near-infrared range. This high damping gives it an important advantage over common semiconductors and thin film solar cell materials, perhaps rivalled only by germanium (Figure 2a).

Strong interaction is here demonstrated between the lowest order, dipolar-like LSPR of the SnS-coated array and the lowest order Fabry−Perot mode of the nanocavity. It is argued that mode equilibration resulting from this coupling facilitates the dual-band, near-perfect absorption observed and that this may more generally be useful for fulfillment of a specific optical condition (such as optical impedance matching, perfect transmission, or perfect reflection) over two or more spectral locations. SnS is identified as one of the strongest semiconductor candidates toward the application in ultrathin plasmonic solar cells.
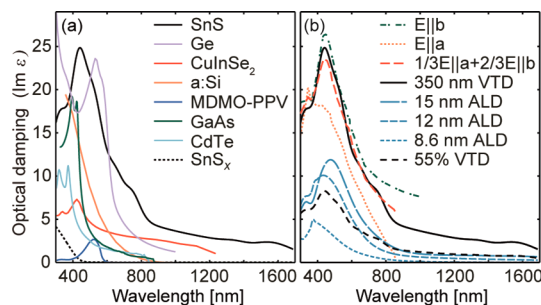
Gold nanodot arrays coated with a range of SnS thicknesses were also analyzed by spectroscopic ellipsometry, to yield their effective thickness (d_{eff}) and effective permittivity [$\varepsilon_{eff} = N_{eff}^2 = (n_{eff} + ik_{eff})^2$ where N_{eff}, n_{eff}, and k_{eff} are the effective complex
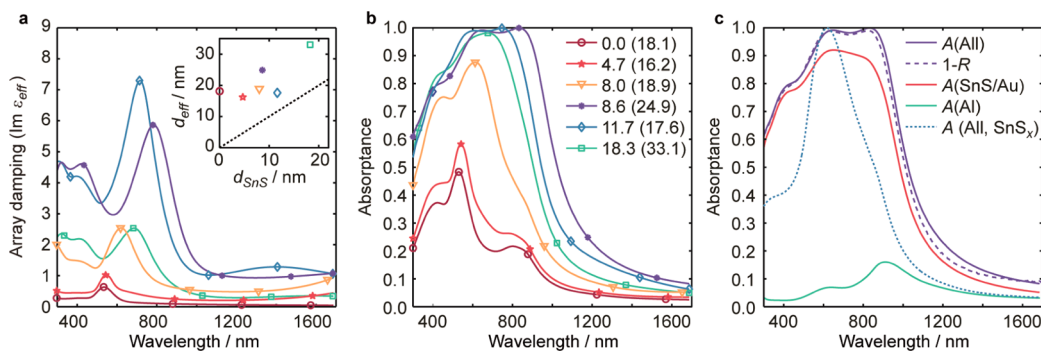
Figure 3. (a) Effective optical damping (Im ε_{eff}) of SnS-coated Au nanodot arrays. The inset shows (by symbols) the corresponding effective thicknesses (d_{eff}) of the arrays versus the SnS thicknesses (d_{SnS}) on parallel-processed Si(100) samples. The dotted line $d_{eff} = d_{SnS}$ gives the asymptotic slope expected for thick SnS coatings. (b) Coated Au nanodot array sample absorptance (A) at normal incidence, with the SnS thicknesses deposited on Si(100) and the effective thicknesses (in parentheses) of the coated arrays indicated in nanometer units. (c) Overall [A(All)] and single-layer absorptance [A(SnS/Au) and A(Al)] in sample with d_{eff} = 24.9 nm, compared to its measured normal incidence reflectance (R). The overall absorptance of a sample with an identical Au nanodot array but a SnS_x coating with $x \approx 2$ is shown for comparison [A(All, SnS_x)].

refractive index, refractive index, and extinction coefficient, respectively]. This type of analysis is applicable since all characteristic length scales within the layer are much below the wavelength of light,[28] with little scattering of light by the Au nanodots.[30] Further, the coated array is highly uniform over macroscopic (~cm) distances, with effective thickness variations determined to a few ångströms. Together with the large number of nanodots interacting coherently with the light, this results in uniform reflection and small depolarization. SE has previously been shown useful for the analysis of many similar systems.[9,31−33] In the ellipsometry model employed here, the properties of the 55 nm thick SiO$_2$ spacer and the reflective Al layer were previously reported.[9] Kramers−Kronig consistent optical properties were imposed for all layers, including the coated array. The ellipsometry analysis is further described in Methods, and an example fit to the ellipsometric data is provided in Supporting Figure S1. The resulting effective damping (Im ε_{eff}) is shown for a bare Au nanodot array and a few SnS-coated arrays in Figure 3a. Without the SnS coating, the array has an effective thickness of 18 nm, similar to the particle layer height determined from TEM.

The peak in the effective damping signifies the localized surface plasmon resonance of the array; see further below. Initially, the effective thickness of the array is seen to depend only weakly on the coating thickness, while the LSPR peak increases strongly in amplitude and width. The effective damping reaches a maximum for an intermediate coating thickness. This behavior can be qualitatively understood since when the SnS coating thickness increases, the polarizability of the Au nanodots is enhanced and contributes more to the effective damping, while when the effective layer thickness increases, the volume fraction occupied by the Au nanodots decreases and their influence is diluted.[9]

The SnS coating has a correspondingly strong influence on the sample absorptance, calculated at normal incidence by means of the transfer matrix method.[34] Assuming full coherence and using the effective thicknesses and permittivities obtained from the SE analysis as inputs, this calculation sums the transversal field components at each interface of the stack, taking multiple internal reflections and phases into account. The overall absorptance is seen to increase strongly upon application of the SnS (Figure 3b), reaching its highest extent for a SnS coating thickness around 8.6 nm. The latter thickness is estimated from a SnS film deposited in parallel on a plain

Si(100) substrate. The corresponding effective thickness of the SnS-coated array is 24.9 nm. As peak broadening is a general consequence of damping, this can be expected due to the high imaginary part of the SnS permittivity. For comparison, a low-damping coating of SnS_x with $x \approx 2$ that was explored in a previous work[9] results in a much narrower absorption band (Figure 3c). Interestingly, some of the most absorbing SnS-coated samples also display a distinct dual peak structure. Focusing on the sample with the 8.6 nm SnS coating, two near-perfect absorption peaks are located at wavelengths of 647 and 832 nm, respectively (Figure 3c). This dual peak is nontrivial, since there is no corresponding feature in the effective damping of the SnS-coated array, which displays only a single, broad resonance peak centered at 756 nm (Figure 3a). To confirm this observation, the specular reflectance at near-normal incidence was measured. This supports the SE result and in particular displays the same dual-peak signature (Figure 3c).

From the near-zero reflectance dips observed, the structure as a whole is necessarily close to being optically impedance matched at the two absorption peaks. This is further elucidated by a comparison of the sample absorptance and the effective optical constants of the coated array on one hand and the requirement for impedance matching on the other (Figure 4). The condition for optical impedance matching may be expressed in the optical constants for the absorber layer (n_{OIM}, k_{OIM}), as shown in Figure 4b after taking the effective thickness and nonideal reflector phase shift into account.[5,9] The deviation of the effective optical constants of the coated array from the impedance matched condition is clearly minimized near the two absorption maxima in Figure 4a.

A single plasmon resonance alone may not give rise to two separate absorption peaks, and there is clearly an offset between the peak positions and the plasmon resonance; the absorption peaks are more or less symmetrically located around the plasmon resonance. Since peak splitting is a well-known effect of mode mixing (hybridization),[35] these observations may be explained by strong coupling of the plasmon resonance to some additional resonance. However, such a resonance cannot be intrinsic to the coated array, as it would then be revealed in its effective extinction coefficient (Figure 4b). Therefore, one may exclude hybridization with excitons of the SnS coating and other resonances of the coated array itself as a leading cause for the peak splitting. The involvement of guided modes (including surface propagating plasmons and waveguided modes) of any
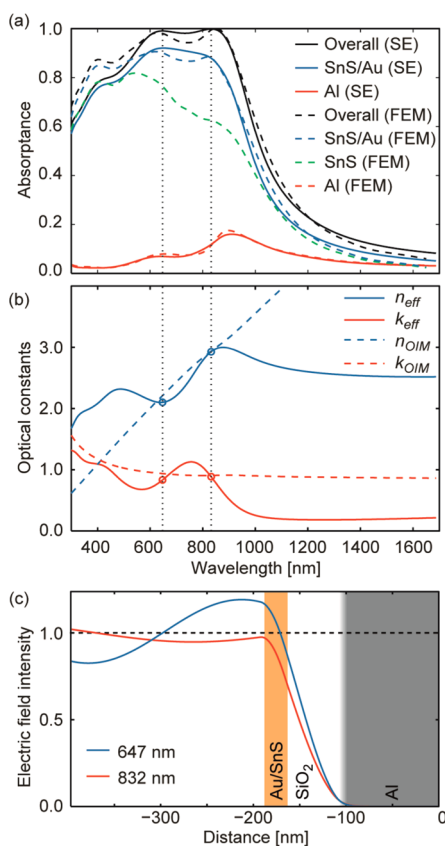
Figure 4. Absorption, optical constants, and field intensity profiles for a sample with d_{eff} = 24.9 nm. (a) Overall and individual layer absorptance obtained from the stratified SE model (transfer matrix method) and from FEM 3D calculations. (b) Comparison of the effective optical constants of the SnS/Au nanocomposite to those of an optically impedance matched absorber layer of the same thickness. (c) Effective electric field intensity profile, $|E|^2/|E_0|^2$, at the two resonance wavelengths indicated. Light is incident from the left.

kind can also be excluded, since the 2-fold absorption peaks are reproduced in transfer matrix calculations using a stratified model with uniform thickness layers that have effective optical constants that are isotropic and homogeneous. Normal incident light cannot be coupled to modes with nonzero lateral propagation in such a one-dimensional structure.

Moreover, it is also noted that the Al interband transitions and the correspondingly enhanced damping of the Al reflector at around 1.5 eV (827 nm) are of little relevance for the dual-peak structure, as the latter is well reproduced even for a plain Drude-like reflector; see further Figure S3 of the SI.

What remains then are the Fabry–Perot resonances of the nanocavity formed by the array/spacer/reflector stack. The transfer matrix calculations show that the two resonance peaks have qualitatively similar field intensity profiles (Figure 4c), with a simple monotonic decay in the nanocavity part of the structure, characteristic of an antisymmetric FP resonance. The absence of nodes excludes the involvement of higher order modes here, in contrast to a previous work,[15] and thus shows that only the lowest order FP mode is involved. One may note that the fringe amplitude in front of the cavity is rather large, because it is $2R^{1/2}$ times the incident field intensity for small reflectance R; a 1% reflectance gives a 20% fringe amplitude relative to the incident field intensity. The identification of the LSPR and FP modes as the only modes of relevance, together

with the observed offset between the LSPR and the two absorption peaks, implies that strong coupling between the lowest order FP and LSPR modes and the resulting hybridized modes are responsible for the dual-band near-perfect absorption.

To gain further insight into these optical resonance modes, a three-dimensional (3D) model was developed for the most absorbing sample and the electromagnetic fields were calculated using the finite element method (FEM). In the model, the geometry and optical properties of the gold nanodots were taken from previous work along with the properties of all sublayers,[9] leaving only the distribution and optical constants of the SnS coating to be determined. The latter were obtained from the effective medium approximation in Figure 2b, as further described in Methods. A cross section of the final geometry is shown in Figure 1c.

The FEM-calculated absorptance reproduces the dual-peak structure (Figure 4a). The calculations also show that only a single, dipolar plasmon resonance of the coated array is involved, as the internal field intensity distribution in the metal part of the structure is essentially homogeneous at both absorption peaks, differing importantly only in phase relative to the external field (Figure 5a). The plasmon-induced field external to the metal particle adds constructively to the external (driving) field at the low-frequency, 850 nm peak (measured at 832 nm) and shifts gradually to a lagging response at the high-
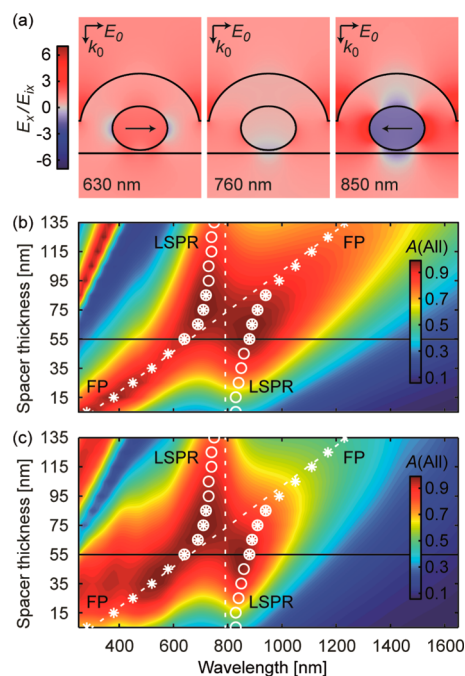

Figure 5. (a) Normalized electric field distribution E_x/E_0, where E_x is the field component along the direction of the incident field E_0 of a plane wave propagating along k_0. Arrows show the internal field direction in the Au nanodots. The resonance wavelengths of the FEM model plus one intermediate wavelength are shown. (b) Overall absorptance versus spacer thickness, for a sample with d_{eff} = 24.9 nm, but with optical constants of the SnS coating fixed to the values at 756 nm wavelength. The black horizontal line indicates the spacer thickness (55 nm) of the actual sample. The predominant character of the modes is indicated by circles and stars as denoted, with overlapping symbols representing strongly hybridized modes. (c) Same as in (b), but with wavelength-dependent optical constants of the SnS coating.

frequency, 630 nm peak (measured at 647 nm). These are all characteristic features of a single dipolar LSPR near its center frequency.

Having confirmed the dipolar LSPR mode of the array and the lowest order FP mode of the optical nanocavity as two basic modes of the structure, we further investigate whether strong coupling between these modes is responsible for the absorption peak splitting around the LSPR. To this end, the overall absorptance was calculated for a range of spacer thicknesses (Figure 5b). The SnS permittivity was first kept fixed to its value at the LSPR peak (756 nm wavelength) in these calculations, in order to more clearly distinguish the effect of the LSPR-FP coupling alone. In the spectral region of interest the actual situation is well approximated, and two absorption branches are clearly distinguished. The high-energy branch is dominated by the cavity mode for short wavelengths, as evidenced by its linear dependence on the spacer thickness. For longer wavelengths, this branch transitions into an LSPR-dominated mode and varies only slightly with the spacer thickness. Correspondingly, the low-energy branch transitions from the LSPR-dominated mode into the nanocavity mode toward longer wavelengths. In the intermediate region, anticrossing of the two branches is clearly observed. As this behavior is a trademark of strongly coupled oscillators, it supports the formation of two hybridized LSPR−nanocavity modes. A calculation with the wavelength-dependent optical constants for the SnS coating shows the same general anticrossing pattern, although it is now convoluted with the spectral dependence of the SnS properties (Figure 5c).

For ease of comparison, the ridges identified from the fixed optical constants calculation is overlaid also in Figure 5c. For the sample conditions with a 55 nm spacer (black line), the resonances have strong components of both modes, although with a slight overweight of the FP mode for the short- and the LSPR mode for the long-wavelength peak, respectively. Consistently, the field distributions in Figure 5a are more uniform, FP-like at 630 nm and more dipolar, LSPR-like at 850 nm. By varying the spacer thickness, it is possible to control the degree of mixing and the nature of these modes and perhaps more closely match the condition for optical impedance matching, as this does depend somewhat on wavelength (Figure 4b).

For light harvesting applications, it is important to distinguish the (useful) absorption in the semiconductor part of the structure from heat dissipation in the Au nanodots and elsewhere. By integrating the local absorption rate found from the FEM model, the estimated absorptance in the SnS is obtained (Figure 4a). A weighted integration shows that 60% of the AM1.5G photons with energies exceeding the SnS band gap (wavelengths from 300 to 1240 nm) may contribute to photocurrent generation, assuming an efficient scheme for utilizing the SnS band-gap excitations. From similar calculations, 12% and 8% of the photons are lost to heat in the Au nanodots and Al back reflector, respectively. The remaining 20% are reflected. The SnS absorption corresponds to a short-circuit current of 29 mA/cm^2, and the ideal, upper limit solar energy conversion efficiency is therefore 19% based on a 1.0 eV band gap.[5,36] These results are reasonably robust (see the SI, Figure S4), and they clearly depend on both the nanocavity and the LSPR modes (see Figure S5).

The exchange of energy between two basic resonance modes is known as vacuum Rabi oscillations in quantized systems. The Rabi splitting energy is characterized by the minimum energy

difference of the anticrossing modes, here estimated to be 400 meV. This splitting corresponds to 24% of the plasmon resonance energy, which is surprisingly large given that the strong damping in the system acts to reduce it.[37] The splitting is indicative of an exceptionally strong coupling, especially when considering the all-inorganic absorber and the semiopen cavity structure used here. In fact, it is not far from the highest values reported for any optical system to our knowledge, namely, the exciton−cavity coupling of around 32% achieved in a considerably different metal/absorber/metal configuration with an organic absorber.[38]

With reference to Figure 5b, it is clear that when the spacer thickness increases, there is a gradual transition of the short-wavelength branch from an FP- to a more LSPR-like behavior and the other way around for the long-wavelength branch. At some point, the two mixed modes will both be equally influenced by the two basic modes and share properties such as damping (peak width) and oscillator strength.[37] This means that by tuning one of the hybrid modes to the condition for, in the present case, optical impedance matching, the other will nearly also fulfill the same condition. In this respect, strongly coupled systems have an advantage over weakly or noncoupled systems. Namely, well-mixed resonances can simultaneously be tuned to optimal conditions within the same geometry. This type of mode equalization may be generalized to include strong coupling between multiple resonances, to match more than two resonances to specific conditions. For instance, near-perfect transmission, reflection, or absorption could be generated at multiple spectral locations.

Although strong coupling between FP and LSPR modes may be observed in similar systems, the exceptional strength of this coupling is here facilitated by the particular optical properties of the SnS coating. The high refractive index (∼5) of SnS leads to strong optical confinement (internal reflection) and population of the nanocavity mode. The confined FP field overlaps strongly with the LSPR near-field distribution, and hence a strong near-field coupling results. This reasoning is in line with the sharp change of the effective field intensity at the front surface of the absorber layer (Figure 4c), which shows that this interface is what mainly confines the hybridized plasmon−nanocavity modes. A similar level of confinement and strong coupling could also be accomplished with a high metal filling factor in the absorber layer,[15] as is possibly the case in, for instance, the work by Liu et al.[19]

Another important feature of the SnS, as already noted, is its heavy optical damping. As a consequence, although the spectral characteristics are governed by the plasmon−nanocavity interaction, most of the energy is actually transferred to the band-gap excitations of the SnS (Figure 4a) rather than to Joule heating of the Au dots. While this broadband absorption channel couples directly to both the LSPR and FP modes via their near-fields, no spectral signatures of strong interaction—such as the asymmetric Fano resonance lines[39]—are observed here.

To achieve yet stronger coupling, and thereby a broader spectral coverage, further volume confinement of the resonances is a feasible approach. This could be accomplished by denser particle arrays or denser SnS coatings, with effectively higher refractive index and damping. For photovoltaic applications it is therefore of interest to further investigate the nucleation and growth of ultrathin SnS films by ALD and perhaps by other methods as well. It is finally noted that the strong coupling phenomenon is not restricted to particular

array types or even ordered systems; calculations for square arrays give the same results as for hexagonal arrays as long as the metal filling factor is preserved. Because the coated arrays behave as effective media, their properties do not depend on details of the microstructure, and disordered distributions of more heterogeneous metal particles can be expected to work equally well as long as inhomogeneous broadening is not too high and the nanocomposite layer is uniform on the wavelength scale.

■ CONCLUSION

Very strong interaction is observed between the localized surface plasmon resonance of a SnS-coated Au nanodot array and the lowest order Fabry−Perot resonance of the nanocavity it constitutes a part of. The resulting hybridized modes are heavily damped by the band-to-band transitions of the SnS coating and result in two broad but distinct near-perfect absorption peaks. The dual-band absorption is facilitated by the strong coupling, as this allows for the two basic LSPR and FP modes to have an equal influence on the resulting hybridized modes, such that these share key similarities and may be simultaneously impedance matched. Via this mode equilibration mechanism, strong coupling may be useful for an extensive range of optoelectronic applications where it is desirable to match specific conditions for broad- or dual-band absorptance, reflectance, or transmittance in a compact, simple geometry. The present results emphasize its application to ultrathin absorber layers for photovoltaics. Thanks to the exceptionally strong optical damping of SnS, the spectrally averaged absorption in the 10 nm thick SnS coating supports a photovoltaic conversion efficiency of up to 19% under ideal conditions. This result highlights a new direction for the development of both cheap and efficient solar energy conversion on the nanoscale, with SnS as one promising semiconductor candidate. It should, however, be noted that many significant challenges remain, from a deepened theoretical understanding of the conditions for which strong coupling develops in this type of system to its practical implementation in photovoltaic devices.

■ METHODS

Samples of gold nanodot arrays, along with glass and Si(100) substrates, were prepared and coated with ultrathin films of SnS by means of ALD as further described below. Scanning and transmission electron microscopy (SEM and TEM, respectively) indicated that the films contained crystalline grains (Figure 1a and d), especially since crystallographic planes of varying orientations were distinguishable in TEM. However, X-ray diffraction performed on samples with 50 nm thick SnS films resulted in no significant peaks, presumably because the grain sizes were too small.

Substrate Preparation. Gold nanodot array samples were cut from a previously characterized substrate, comprising a 55 nm thick SiO_2 dielectric spacer and a highly reflective, optically thick aluminum layer; see Figure 1b−d. Block copolymer lithography was used to produce the hexagonal gold nanodot array, with a lattice constant of 37.9 nm as previously described.[9] The dots were approximately spheroidal and had, on average, estimated diameters of 16.8 nm and heights of 13.6 nm. Gold nanodot array patterned samples, glass, and Si(100) pieces were cleaned in a UV-ozone chamber shortly before transfer to the ALD reactor for SnS growth.

Tin Monosulfide Deposition. SnS was deposited in an atomic layer deposition process previously developed by Kim and George,[27] where precursors of tin(II) 2,4-pentanedionate [Sn(acac)$_2$, 99.9% purity, Sigma-Aldrich] and hydrogen sulfide were used to deposit tin sulfide. The H_2S was generated in a separate vial through thermal decomposition of thioacetamide (Sigma-Aldrich, >99% purity).[40] The home-built viscous flow reactor, described in more detail elsewhere,[41] was evacuated to a pressure around 100 mTorr, at a 10 sccm flow of nitrogen carrier gas. An online mass spectrometer was used to monitor the gas composition, including the levels of water and oxygen, via a small orifice used for sampling gas downstream of the sample stage. The tin precursor vial and the substrate stage were heated to 110 °C. Deposition was initiated after about 30 min, when the temperatures were equilibrated and any gas contamination levels were low. The ALD cycle consisted of a 1 s tin precursor pulse, followed by a 30 s purging step, a 0.25 s hydrogen sulfide pulse, and another 30 s purge. Between 50 and 500 ALD cycles were typically performed.

The vapor transport deposition and epitaxial growth of SnS on NaCl was detailed in a previous report.[25]

Electron Microscopy. Scanning electron microscopy measurements were performed using an FEI Magellan 400 XHR SEM with 5 kV beam voltage, 25 pA current, and a through-the-lens detector. Samples for transmission electron microscopy were prepared by standard tripod polishing followed by thinning with a Gatan PIPS ion miller. The TEM analysis was conducted at 200 kV on a FEI Tecnai G2 F20 X-TWIN TEM.

Spectroscopic Ellipsometry. Standard spectroscopic ellipsometry measurements were performed using a Woollam M2000 instrument, over wavelengths from 210 to 1687 nm and 65°, 70°, and 75° angles of incidence. The data were analyzed through simple stratified models of the samples, using only uniform, homogeneous, and isotropic layers. The imaginary part of the effective permittivity for the SnS-coated Au nanodot array was modeled using a superposition of oscillator terms, essentially representing absorption in the layer due to various processes. The real part was then obtained through a Kramers−Kronig transform of the imaginary part, plus a pole on each side of the measured range to represent additional absorption unaccounted for by the imaginary part. Thereby, the Kramers−Kronig relation was imposed by construction. Predetermined data or literature data were employed for all sublayers. Only the top layer thickness and permittivity parameters were fitted, by minimizing the root mean squared deviation of the model output from the ellipsometric raw data. For samples of SnS on Si(100), the oscillator model comprised a polynomial spline function (the "psemi-m0" function) and up to seven Gaussian oscillators.

For samples of SnS-coated gold nanodot arrays on SiO_2/Al substrates, the sample model used the previously established properties for the SiO_2 and Al sublayers.[9] Only the effective optical constants and thickness of the SnS-coated gold nanodot array were fitted. This was done by a parametrized oscillator layer comprising one Gaussian, one psemi-m0, and six harmonic oscillators. An example of the resulting fit of this model to the ellipsometric data is given in Figure S1 of the SI.

Reflectance Measurements. The specular reflectance was measured near normal incidence by means of a Hitachi U-4001 spectrophotometer equipped with a 5° specular reflectance attachment. Wavelengths from 300 to 1800 nm were covered in 5 nm steps. Dark and Si reference sample measurements were

made before and after the sample runs were completed. The sample reflectance was then obtained from $R = R_{Si} \times (R_{Sample}^{meas} - R_{Dark}^{meas})/(R_{Si}^{meas} - R_{Dark}^{meas})$, where R_{Sample}^{meas} is the measured but uncalibrated sample reflectance, R_{Dark}^{meas} the (near zero) measured reflectance of a beam trap replacing the sample, R_{Si}^{meas} the measured Si reflectance, and R_{Si} the known reflectance of Si based on tabulated data. The back of the Si was rough, so that specular back reflections were suppressed also for wavelengths above the Si band-gap threshold near 1100 nm.

Modeling by the Finite Element Method. The basic modeling procedure was as previously described[42] and used software from Comsol Multiphysics. The simulation domain included an entrance boundary padded with a perfectly matched layer to simulate its extension to (negative) infinity, while the back boundary used an impedance boundary condition to simulate an optically thick aluminum layer. Periodic boundary conditions were used to model a unit cell for the hexagonal lattice of gold nanodots. Tetrahedral mesh elements were used with their maximum size restricted below 0.5 nm in the critical regions around the Au nanodots. The absolute error from this discretization was estimated to be on the order of 0.01% in the reflectance.

A square lattice gave the same results as the hexagonal one, as long as the particle density (filling factor) was maintained the same, and polarization was of no importance at normal incidence. These are characteristic features of an isotropic effective medium. The same geometry and optical properties as described in an earlier work were used for the gold nanodot arrays and the reflective substrate.[9] This included a surface scattering correction for the gold nanodots as discussed in more detail in the SI.

A conformal SnS coating thickness of 10 nm (Figure 1c) was assumed. In this way, the average height of SnS-coated gold dots approximately agreed with the effective thickness of the coated array, as measured by SE (24.9 nm) and TEM. This choice of coating thickness is also close to the SnS thickness of 8.6 nm extracted for the films deposited on Si in the same ALD run. Given the high roughness of the ALD SnS observed, an effective medium of air and polycrystalline SnS was constructed to represent the average optical properties of the SnS deposited on the arrays in the FEM model. In this coating mixture, the SnS properties were taken from thicker SnS films grown epitaxially by vapor transport deposition,[25] as these closely resemble (and extend) the literature data for compact layers of polycrystalline SnS[29] (see Figure 2b). The isotropic Bruggeman effective medium approximation was investigated for filling factors from 0 to 1, corresponding to an effective damping of the SnS/air coating mixture from 0 up to that of the VTD SnS. The best agreement with the measured absorptance was found for a 0.55 SnS filling factor (see SI, Figure S4). The usage of the Bruggeman effective medium approximation for a nonplanar nanocomposite coating is here merely an averaging procedure without rigorous physical support. However, to the extent that the filling factor is an indication of the actual volume fraction of SnS, it appears quite reasonable when compared to the electron microscopy images of the ALD-deposited films (such as in Figure 1d), which show that the SnS films are very rough. The corresponding effective damping of the mixture is shown in Figure 2b. It is similar to those ALD films of comparable thickness measured on Si(100) substrates, although somewhat higher in the long-wavelength range.

ASSOCIATED CONTENT

Ⓢ Supporting Information

The Supporting Information is available free of charge on the ACS Publications website at DOI: 10.1021/acsphotonics.5b00651.

> Example fit to ellipsometry data, optical properties of gold nanodots and their effect on the sample absorptance, effect of aluminum interband transitions on overall absorptance, effect of coating filling factor on overall and individual layer absorptance, and comparison of the absorption in SnS with and without gold nanodots (PDF)

AUTHOR INFORMATION

Corresponding Authors
*E-mail: carl.hagglund@angstrom.uu.se.
*E-mail: sbent@stanford.edu.

Present Addresses
‡Division of Solid State Electronics, Department of Engineering Sciences, Uppsala University, 75121 Uppsala, Sweden.
∥Waves Audio Ltd., Tel Aviv 6701101, Israel.
#Department of Electrical Engineering, Faculty of Engineering, King Mongkut's University of Technology Thonburi, Bangkok 10140, Thailand.

Author Contributions
⊥G. Zeltzer and R. Ruiz contributed equally.

Notes
The authors declare no competing financial interest.

REFERENCES

(1) Atwater, H. A.; Polman, A. Plasmonics for improved photovoltaic devices. *Nat. Mater.* **2010**, *9*, 205−213.
(2) Gu, M.; Ouyang, Z.; Jia, B.; Stokes, N.; Chen, X.; Fahim, N.; Li, X.; Ventura, M. J.; Shi, Z. Nanoplasmonics: a frontier of photovoltaic solar cells. *Nanophotonics* **2012**, *1*, 235.
(3) Rand, B. P.; Peumans, P.; Forrest, S. R. Long-range absorption enhancement in organic tandem thin-film solar cells containing silver nanoclusters. *J. Appl. Phys.* **2004**, *96*, 7519−7526.
(4) Cai, B.; Jia, B.; Shi, Z.; Gu, M. Near-field light concentration of ultra-small metallic nanoparticles for absorption enhancement in a-Si solar cells. *Appl. Phys. Lett.* **2013**, *102*, 093107.
(5) Hägglund, C.; Apell, S. P. Resource efficient plasmon-based 2D-photovoltaics with reflective support. *Opt. Express* **2010**, *18*, A343−A356.
(6) Hägglund, C.; Apell, S. P.; Kasemo, B. Maximized optical absorption in ultrathin films and its application to plasmon-based two-dimensional photovoltaics. *Nano Lett.* **2010**, *10*, 3135−3141.
(7) Salisbury, W. W. Absorbent body for electromagnetic waves. U.S. Patent 2599944, June 10, 1952.
(8) Tischler, J. R.; Bradley, M. S.; Bulovic, V. Critically coupled resonators in vertical geometry using a planar mirror and a 5 nm thick absorbing film. *Opt. Lett.* **2006**, *31*, 2045−2047.

(9) Hägglund, C.; Zeltzer, G.; Ruiz, R.; Thomann, I.; Lee, H.-B.-R.; Brongersma, M. L.; Bent, S. F. Self-assembly based plasmonic arrays tuned by atomic layer deposition for extreme visible light absorption. *Nano Lett.* **2013**, *13*, 3352−3357.

(10) Song, H.; Guo, L.; Liu, Z.; Liu, K.; Zeng, X.; Ji, D.; Zhang, N.; Hu, H.; Jiang, S.; Gan, Q. Nanocavity enhancement for ultra-thin film optical absorber. *Adv. Mater.* **2014**, *26*, 2737−2743.

(11) Steenhoff, V.; Theuring, M.; Vehse, M.; von Maydell, K.; Agert, C. Ultrathin resonant-cavity-enhanced solar cells with amorphous germanium absorbers. *Adv. Opt. Mater.* **2015**, *3*, 182−186.

(12) Wu, C. H.; Neuner, B.; Shvets, G.; John, J.; Milder, A.; Zollars, B.; Savoy, S. Large-area wide-angle spectrally selective plasmonic absorber. *Phys. Rev. B: Condens. Matter Mater. Phys.* **2011**, *84*10.1103/PhysRevB.84.075102.

(13) Esfandyarpour, M.; Garnett, E. C.; Cui, Y.; McGehee, M. D.; Brongersma, M. L. Metamaterial mirrors in optoelectronic devices. *Nat. Nanotechnol.* **2014**, *9*, 542−547.

(14) Kats, M. A.; Blanchard, R.; Genevet, P.; Capasso, F. Nanometre optical coatings based on strong interference effects in highly absorbing media. *Nat. Mater.* **2013**, *12*, 20−24.

(15) Gupta, S. D. Strong-interaction-mediated critical coupling at two distinct frequencies. *Opt. Lett.* **2007**, *32*, 1483−1485.

(16) Hedayati, M. K.; Javaherirahim, M.; Mozooni, B.; Abdelaziz, R.; Tavassolizadeh, A.; Chakravadhanula, V. S. K.; Zaporojtchenko, V.; Strunkus, T.; Faupel, F.; Elbahri, M. Design of a perfect black absorber at visible frequencies using plasmonic metamaterials. *Adv. Mater.* **2011**, *23*, 5410−5414.

(17) Zhao, H.; Guo, Q.; Xia, F.; Wang, H. Two-dimensional materials for nanophotonics application. *Nanophotonics* **2015**, 410.1515/nanoph-2014-0022.

(18) Hägglund, C.; Apell, S. P. Plasmonic near-field absorbers for ultrathin solar cells. *J. Phys. Chem. Lett.* **2012**, *3*, 1275−1285.

(19) Liu, Z.; Liu, X.; Huang, S.; Pan, P.; Chen, J.; Liu, G.; Gu, G. Automatically acquired broadband plasmonic-metamaterial black absorber during the metallic film-formation. *ACS Appl. Mater. Interfaces* **2015**, *7*, 4962−4968.

(20) Hedayati, M. K.; Fahr, S.; Etrich, C.; Faupel, F.; Rockstuhl, C.; Elbahri, M. The hybrid concept for realization of an ultra-thin plasmonic metamaterial antireflection coating and plasmonic rainbow. *Nanoscale* **2014**, *6*, 6037−6045.

(21) Mann, S. A.; Garnett, E. C. Extreme light absorption in thin semiconductor films wrapped around metal nanowires. *Nano Lett.* **2013**, *13*, 3173−3178.

(22) Aydin, K.; Ferry, V. E.; Briggs, R. M.; Atwater, H. A. Broadband polarization-independent resonant light absorption using ultrathin plasmonic super absorbers. *Nat. Commun.* **2011**, *2*, 517.

(23) Sinsermsuksakul, P.; Heo, J.; Noh, W.; Hock, A. S.; Gordon, R. G. Atomic layer deposition of tin monosulfide thin films. *Adv. Energy Mater.* **2011**, *1*, 1116−1125.

(24) Banai, R. E.; Lee, H.; Motyka, M. A.; Chandrasekharan, R.; Podraza, N. J.; Brownson, J. R. S.; Hom, M. W. Optical properties of sputtered SnS thin films for photovoltaic absorbers. *IEEE J. Photovolt.* **2013**, *3*, 1084−1089.

(25) Wangperawong, A.; Herron, S. M.; Runser, R. R.; Hägglund, C.; Tanskanen, J. T.; Lee, H.-B.-R.; Clemens, B. M.; Bent, S. F. Vapor transport deposition and epitaxy of orthorhombic SnS on glass and NaCl substrates. *Appl. Phys. Lett.* **2013**, *103*, 052105.

(26) Sinsermsuksakul, P.; Sun, L.; Lee, S. W.; Park, H. H.; Kim, S. B.; Yang, C.; Gordon, R. G. Overcoming efficiency limitations of SnS-based solar cells. *Adv. Energy Mater.* **2014**, *4*, 1400496.

(27) Kim, J. Y.; George, S. M. Tin monosulfide thin films grown by atomic layer deposition using tin 2,4-pentanedionate and hydrogen sulfide. *J. Phys. Chem. C* **2010**, *114*, 17597−17603.

(28) Niklasson, G. A.; Granqvist, C. G.; Hunderi, O. Effective medium models for the optical properties of inhomogeneous materials. *Appl. Opt.* **1981**, *20*, 26−30.

(29) Eymard, R.; Otto, A. Optical and electron-energy-loss spectroscopy of GeS, GeSe, SnS, and SnSe single crystals. *Phys. Rev. B* **1977**, *16*, 1616−1623.

(30) Jain, P. K.; Lee, K. S.; El-Sayed, I. H.; El-Sayed, M. A. Calculated absorption and scattering properties of gold nanoparticles of different size, shape, and composition: applications in biological imaging and biomedicine. *J. Phys. Chem. B* **2006**, *110*, 7238−7248.

(31) Losurdo, M.; Hingerl, K. *Ellipsometry at the Nanoscale*; Springer, 2013; p 730.

(32) Toudert, J. Spectroscopic ellipsometry for active nano- and meta-materials. *Nanotechnol. Rev.* **2014**, *3*, 223−245.

(33) Mendoza-Galván, A.; Järrendahl, K.; Dmitriev, A.; Pakizeh, T.; Käll, M.; Arwin, H. Optical response of supported gold nanodisks. *Opt. Express* **2011**, *19*, 12093−12107.

(34) Born, M.; Wolf, E. *Principles of Optics: Electromagnetic Theory of Propagation, Interference and Diffraction of Light*; Cambridge University Press, 1999.

(35) Haroche, S.; Raimond, J.-M. *Exploring the Quantum: Atoms, Cavities, and Photons*; Oxford University Press: Oxford, GBR, 2006.

(36) Bolton, J. R.; Archer, M. D. Requirements for ideal performance of photochemical and photovoltaic solar energy converters. *J. Phys. Chem.* **1990**, *94*, 8028−8036.

(37) Törmä, P.; Barnes, W. L. Strong coupling between surface plasmon polaritons and emitters: a review. *Rep. Prog. Phys.* **2015**, *78*, 013901.

(38) Schwartz, T.; Hutchison, J. A.; Genet, C.; Ebbesen, T. W. Reversible switching of ultrastrong light-molecule coupling. *Phys. Rev. Lett.* **2011**, *106*, 196405.

(39) Luk'yanchuk, B.; Zheludev, N. I.; Maier, S. A.; Halas, N. J.; Nordlander, P.; Giessen, H.; Chong, C. T. The Fano resonance in plasmonic nanostructures and metamaterials. *Nat. Mater.* **2010**, *9*, 707−715.

(40) Bakke, J. R.; King, J. S.; Jung, H. J.; Sinclair, R.; Bent, S. F. Atomic layer deposition of ZnS via in situ production of H2S. *Thin Solid Films* **2010**, *518*, 5400−5408.

(41) Mullings, M. N.; Hägglund, C.; Bent, S. F. Tin oxide atomic layer deposition from tetrakis(dimethylamino)tin and water. *J. Vac. Sci. Technol., A* **2013**, *31*, 061503.

(42) Hägglund, C.; Zäch, M.; Petersson, G.; Kasemo, B. Electromagnetic coupling of light into a silicon solar cell by nanodisk plasmons. *Appl. Phys. Lett.* **2008**, *92*, 053110.